SAND2019-5687C

Revisiting Bachalo-Johnson: The Sandia Axisymmetric Transonic Hump and CFD Challenge

Kyle P. Lynch[1], Nathan E. Miller[2], Matt F. Barone[3], Steven J. Beresh[4], Russell W. Spillers[5], John F. Henfling[6], and Melissa M. Soehnel[7]
Sandia National Laboratories, Albuquerque, NM

A new wind tunnel experiment is underway to provide a comprehensive CFD validation dataset of an unsteady, transonic flow. The experiment is based on the work of Bachalo and Johnson; an axisymmetric model with a spherical hump is tested at a transonic Mach number. The flow is turbulent approaching the hump and becomes locally supersonic at the apex. This leads to a shock-wave/boundary-layer interaction, an unsteady separation bubble, and flow reattachment downstream. A suite of diagnostics characterizes the flow: oil-flow surface visualization for shock and reattachment locations, particle image velocimetry for mean flow and turbulence properties, fast pressure-sensitive paint for model pressure distributions and unsteadiness, high-speed Schlieren for shock position and motion, and oil-film interferometry for surface shear stress. This will provide a new level of detail for validation studies; therefore, a blind comparison, or 'CFD Challenge' is proposed to the community. Participants are to be provided the geometry, incoming boundary layer, and boundary conditions, and are free to simulate with their method of choice and submit their results. A blind comparison will be made to the new experimental data, with the goal of evaluating the state of various CFD methods for use in unsteady, transonic flows.

I. Introduction

There is a continued emphasis on improving CFD predictions for separated, smooth-body, transonic flows. These flows contain unsteady shock and recirculation regions that challenge model-based approaches such as RANS, DES, LES, among others. Refining these models, or proposing new approaches, requires experimental datasets across many test cases to assess their accuracy and generality. These test cases should be conceptually simple with well-defined boundary conditions. The value of community verification and validation (V&V) resources for CFD has been highlighted in the NASA CFD Vision 2030 Study [1], which points to the example of the NASA Turbulence Modeling Resource website. This website contains numerous turbulence model V&V cases, including the axisymmetric transonic hump experiment described below. Transonic shock-induced separation has also been identified as an important set of physics to be captured within NASA's Revolutionary Computational Aerosciences Technical Challenge [2].

The classic axisymmetric transonic hump test case of Bachalo and Johnson [3] consists of a spherical hump on a cylindrical body aligned with the wind tunnel operating at a high subsonic Mach number. A turbulent boundary layer develops along the cylindrical body, which accelerates as it approaches the hump. The flow becomes supersonic near the apex of the hump, forming a weak shock that imposes an adverse pressure gradient onto the incoming boundary layer. This causes it to separate, forming an unsteady separation bubble downstream of the hump which later undergoes an unsteady reattachment. An oil-flow visualization photo of the original test is shown in figure 1. This simple

[1] Senior Member of the Technical Staff, Aerosciences Department. Corresponding author: klynch@sandia.gov.
[2] Senior Member of the Technical Staff, Aerosciences Department.
[3] Principal Member of the Technical Staff, Aerosciences Department.
[4] Distinguished Member of the Technical Staff, Aerosciences Department.
[5] Principal Technologist, Aerosciences Department.
[6] Principal Test Operations Engineer, Aerosciences Department.
[7] Test Operations Engineer, Aerosciences Department.

Sandia National Laboratories is a multimission laboratory managed and operated by National Technology & Engineering Solutions of Sandia, LLC, a wholly owned subsidiary of Honeywell International Inc., for the U.S. Department of Energy's National Nuclear Security Administration under contract DE-NA0003525. This paper describes objective technical results and analysis. Any subjective views or opinions that might be expressed in the paper do not necessarily represent the views of the U.S. Department of Energy or the United States Government.

geometry is attractive for numerous reasons: first, axisymmetry removes questions related to sidewall interference for an equivalent 2D case; second, it remains a simple geometry for simulation purposes; finally, the captured physics are directly applicable to numerous industry applications, for example, aircraft wings at cruise condition. Therefore, the case is a good candidate for transonic CFD validation.

The Bachalo and Johnson geometry was tested in the NASA Ames 2 ft. x 2 ft. and 6 ft. x 6 ft. transonic facilities and comprised multiple diagnostics: surface oil-flow visualization, Schlieren/interferometric imaging, an array of surface pressure taps, and a traversing laser-Doppler anemometer (LDA). This allowed for measurement of the mean surface pressure coefficient, separation bubble size, mean velocity and turbulent stresses, and some derived properties such as turbulent mixing length. However, as noted by Spalart et al. [4], in the thirty years since its publication, no corroboration of the experimental data has been performed. Furthermore, this experiment did not produce data on skin-friction, and only limited data on flow unsteadiness, shock location, and higher-order turbulent statistics. An additional omission in the experiment was a detailed characterization of the inflow conditions such as freestream turbulence intensity, which is crucial for computational validation studies.

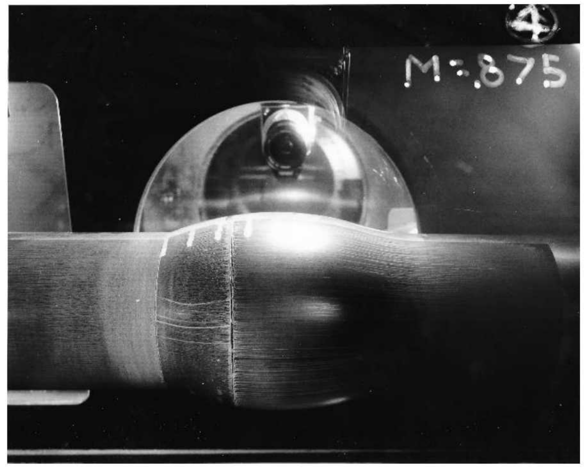

Figure 1. Oil-flow visualization of the Bachalo and Johnson experiment [3] conducted in the NASA Ames 2 ft x 2 ft tunnel. Flow is from right to left. Photo from Langley Turbulence Modeling Resource [4].

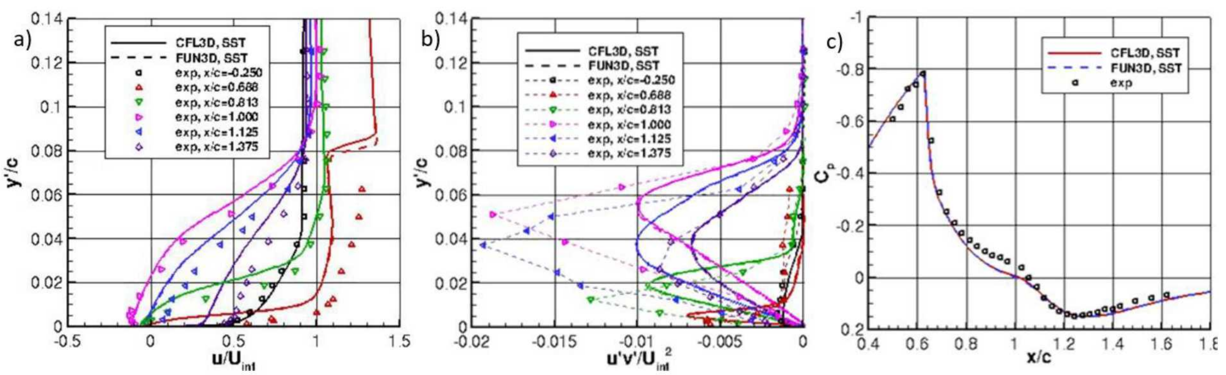

Figure 2. Comparisons of RANS simulations with experimental data. a) mean velocity profiles; b) Reynolds shear stress; c) surface pressure coefficient. Comparisons of the CFL3D and FUN3D codes run using the Menter Shear Stress Transport (SST) turbulence model. Experimental data from Bachalo and Johnson [3]. Figures from the NASA turbulence modelling resource website [4].

Increased attention has been given to the test case recently due to the limited ability of simulations to match the experimental data and the scatter between simulation approaches. As an example, a comparison is shown in figure 2 where RANS simulations using the SST turbulence model. The experimental velocity profiles are noticeably less full, and the measured Reynolds stresses are far higher than the corresponding predictions from simulations. At some locations, the measured Reynolds shear stresses are nearly twice the simulated results. The lower Reynolds stress of the simulations reduces the momentum transfer into the separation region and leads to an increased velocity deficit. These behaviors are common not just in the axisymmetric flow case, but also in the NASA 2D hump case as noted by Rumsey et al. [5].

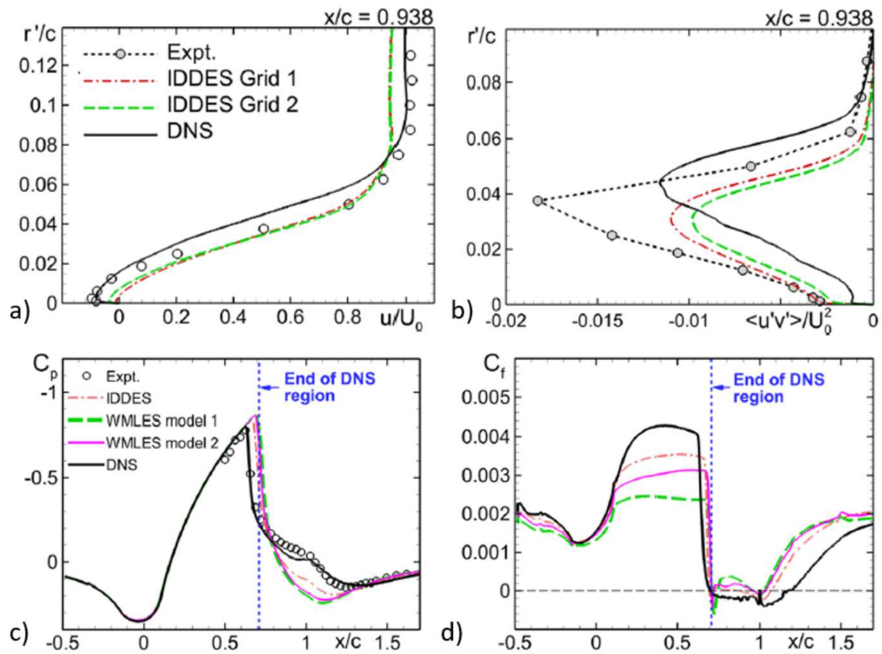

Figure 3. Comparisons of unsteady simulations with experimental data. a) Mean velocity profiles. b) Reynolds shear stress profiles; c) surface pressure coefficient; d) surface skin friction coefficient. Acronyms: Direct Numerical Simuation (DNS), Improved Delayed Detached-Eddy Simulation (IDDES), and Wall-Modelled Large-Eddy Simulations (WMLES). 'End of DNS region' specifies a switch from DNS to IDDES. Experimental data from Bachalo and Johnson [3]. Figures from Spalart et al. [5].

The limited accuracy of RANS and its inability to describe unsteady flow properties has motivated the use of scale-resolving approaches for these separated-flow cases. However, large discrepancies still exist when applying wall-modeled LES, wall-resolved LES, DES, and a partial DNS. In figure 3, comparisons are shown from the simulations of Spalart et al. [4]. The simulations disagree on the predicted shock location, which leads to incorrect flow separation and reattachment. The local rise in pressure coefficient at x/c = 1, associated with flow reattachment, is not captured by many of the approaches. The Reynolds stresses also remain significantly lower than the experimental values, and there are substantial differences in skin-friction coefficient. Unfortunately, there is no experimental skin friction data to compare to. The only approach correctly predicting the shock location is a partial DNS; however, the scale of the calculation is unrealistic for design purposes. These discrepancies raise a desire for additional experimental data to help explain the observations. The situation may be best summarized by Spalart et al. [4],

> *"…the high level of post-separation Reynolds stress measured is considered a clear challenge to RANS models, so that its confirmation is of great interest…A repeat experiment at [lower] Reynolds number and with modern instrumentation would also have great value…"*

This work proposes to revisit the Bachalo-Johnson experiment, with three primary goals: first, to corroborate data on surface pressure, velocity field, and turbulent statistics; second, to apply modern diagnostic techniques such as particle image velocimetry, fast pressure-sensitive paint, and oil film interferometry to quantify the velocity field, unsteady pressure, and surface shear stress; and third, to run the experiment at a lower Reynolds number that is more tractable for high-fidelity computations. Sections 2 and 3 discusses the experimental effort in more detail. Besides the experimental effort, a 'CFD challenge' is being organized, where a blind comparison of simulation efforts is to be made against the new experimental data. Sections 4 and 5 provide detail on simulation efforts from the Sandia team and explain the structure and goals of the challenge.

II. Model Design

The experiment is run in the Sandia Trisonic Wind Tunnel (TWT). The TWT is a blowdown-to-atmosphere facility using air as the test gas with interchangeable test sections. It can achieve subsonic Mach numbers from 0.5 to 1.3 using a variable downstream choke. The test section is a rectangular duct of dimensions 12 in × 12 in enclosed within a plenum to accommodate ventilated test section configurations. The TWT has a run time of 30–40 sec with 20–30 min between runs. For transonic operation, the stagnation pressure can be varied between approximately 16-35 psig, and reservoir heating maintains a stagnation temperature approximately 160-170 °F during a run. Either solid or porous walls may be used; for this experiment, solid walls are chosen to provide a simplified boundary condition for simulations. This poses geometrical restrictions related to tunnel blockage as discussed below.

The TWT is smaller than the NASA Ames 6 ft x 6 ft and 2 ft x 2 ft tunnels used by Bachalo and Johnson [3]. For the 6 ft x 6 ft tunnel, solid walls were used, and for the 2 ft x 2 ft tunnel, the side walls were solid, and the top/bottom walls were porous. Uzun and Malik [6] have noted that there is a considerable effect of the tunnel size and wall porosity on the flow properties; they compared the results from [3] taken in the 2 ft x 2 ft tunnel with the 6 ft x 6 ft data contained in the earlier paper of Horstman and Johnson [7] and found the latter with a 20-27.5% increase in separation bubble size. These differences are expected to be even more significant for the 1 ft x 1 ft cross-section of the TWT; therefore, we caution that this experiment is *not* meant to be an exact replica of Bachalo-Johnson, but a standalone, separate experiment containing similar flow physics subjected to tunnel wall effects that should be included in any modeling or validation effort.

The reduced scale of the wind tunnel requires a scaled-down model. Uzun and Malik [6] describe geometric ambiguities in the model definition given by Bachalo and Johnson, particularly regarding the intersection of the hump with the model. Therefore, an analytical definition of the geometry is proposed; a schematic is given in figure 4.The geometry consists of a cylindrical body of diameter d capped by an elliptical nose of length a. At location a_t, a step of height t fixes the transition location. Following the nose is a constant-diameter forebody of length b. The hump is defined as a circular section of radius R_1 and chord c. It intersects the forebody using a circular fillet of radius R_2 tangent to both the forebody and hump. The hump intersects a constant-diameter afterbody with no fillet, and the afterbody continues length e to the sting mount of the wind tunnel.

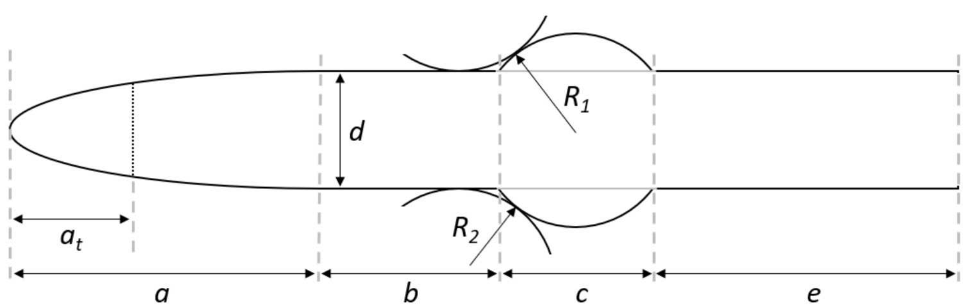

Figure 4. Schematic diagram of model. Flow is from left to right.

The actual values of the geometry as well as the tunnel wall contour are to be released at AIAA SciTech 2020 when the validation challenge begins (see section 5 for more details). The tunnel conditions and geometry quantities are defined to match features of the Bachalo-Johnson configuration such as an incoming Mach number of 0.875, while some additional geometrical constraints are imposed to prevent wind tunnel blockage at the high Mach number. Based on this geometry and the tunnel operational envelope, the target Reynolds number based on chord c is 1 million. A photo of the model within the TWT is shown in figure 5. It is machined from 7075-T6 aluminum and anodized black to reduce laser flare. It is sting mounted over 8 chord lengths downstream of the hump, and far upstream of the tunnel choke location.

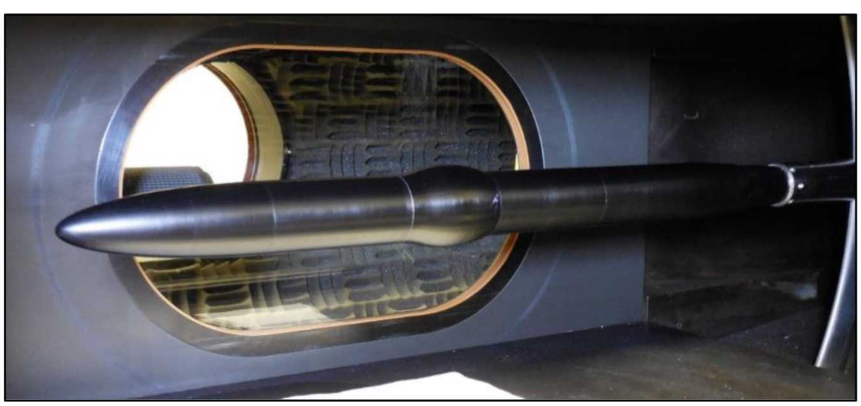

Figure 5. Photo of model in Sandia Trisonic Wind Tunnel.

III. Representative Measurement Results

A. Tunnel Pressure Distribution

The use of a solid-wall test section results in a significant non-uniform pressure distribution along the wall compared to a porous-wall test section. The steady distribution was measured using a Pressure Systems International (PSI) System 8400 with a 64-port electronic pressure scanner connected to 32 uniformly-distributed static pressure taps (0.5 in spacing) along the test section wall and a tap in the stagnation chamber. Calibration was performed prior to each run.

An example of the nonuniformity in the Mach number distribution is shown in figure 6. Due to model blockage and boundary layer growth on the tunnel wall and model, the Mach number increases between 5-10% at the streamwise stations corresponding to the model. The influence of the hump is clearly visible and causes a local rise in the Mach number. As the upstream Mach number increases, a nearly-choked condition is created, limiting the upstream Mach number for this model size.

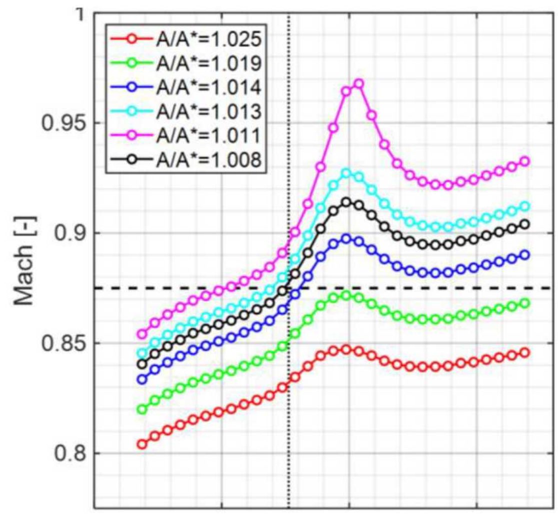

Figure 6. Tunnel wall Mach number distribution as measured from the ratio of wall pressure taps and the stagnation pressure. Various lines correspond to different tunnel choke conditions.

The nonuniformity makes the definition of freestream flow conditions ambiguous. The freestream pressure and Mach number are defined herein as the condition at the tunnel wall at a streamwise station corresponding to $x/c = 0$. This is illustrated with the crosshair in figure 6. For the target condition of $M_\infty = 0.875$, there is margin to prevent the tunnel from operating in a choked condition.

B. High-Speed Schlieren

A standard Z-type Schlieren arrangement is used for measuring the shock location and unsteadiness. The light source is a Cavitar Cavilux Smart 400W laser, which is a pulsed, supercontinuum laser source emitting at 648 +/- 10 nm. It is capable of repetition rates exceeding 1 MHz, but is used at 20 kHz for this experiment to achieve sufficient pulse energy for the large field of view. Pulses of 100 ns duration effectively freeze the unsteady flow structures. A Photron SA-Z camera (1024 x 1024 px at 20 kHz) is used for imaging, and a vertical knife-edge is used to accentuate the shock features occurring over the hump. Example instantaneous and average images are shown in figure 7.

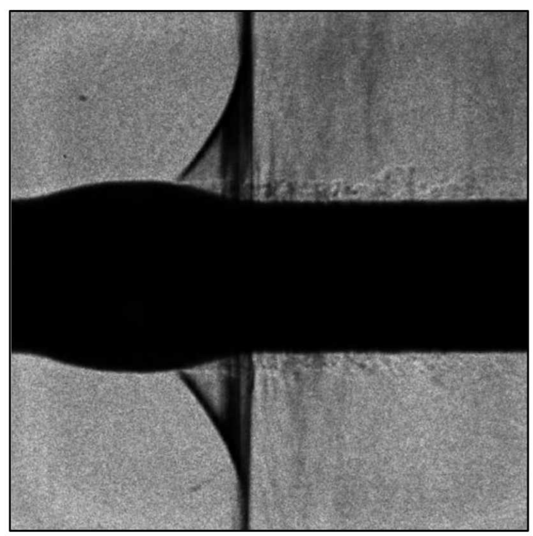

Figure 7. Example image from Schlieren image sequence.

The most prominent feature in the images is the curved shock over the downstream portion of the hump. This is qualitatively similar to the synthetic Schlieren reported by Spalart et al. [4] and Uzun and Malik [6]. The shock position far from the model is nearly stationary; however, there is increased unsteadiness near the shock foot that was not resolved for the current paper. Immediately following the shock foot is a visible shear layer indicating flow separation. Further downstream is a vertical shock feature; this is a consequence of the line-of-sight integration of the Schlieren method and the axisymmetry of the shock structure. Finally, the structures generated in the separated shear layer are shown to move downstream along the length of the model. The final data set will include calibrated Schlieren results, amenable to comparison with synthetic Schlieren data.

C. Surface Oil-Flow Visualization

A simple oil-flow visualization setup is employed for measuring the time-average shock and reattachment locations and evaluating their axisymmetry. The model is sprayed with Zyglo ZL-60D aerosol penetrant and illuminated using a pair of ISSI LM2X-DM-400 ultraviolet LED lamps. The fluorescence is imaged by a Point Grey Blackfly-S camera during the run; all averaging is performed on images acquired during the run time. A two-part camera calibration is performed, first determining the intrinsic and extrinsic camera parameters from a checkerboard target, and then calibrating the camera pose using a set of fiducial marks placed on the model at various streamwise and azimuthal positions. The image data are then mapped onto an unwrapped version of the geometry for inspection on streamwise position/azimuth angle axes.

A set of processed images and a feature map, given without scaling information, is shown in figure 8. The freestream Mach number is varied to compare to the data of Bachalo and Johnson [3] and Horstman and Johnson [7]. The latter used a similar axisymmetric model within the NASA Ames 6 ft x 6 ft transonic tunnel. The shock location is well-matched between all experiments, appearing to either be constant or weakly varying with freestream Mach number. At M = 0.85, there is a clear demarcation between the shock and separation locations that is found in all experiments. However, beginning at and above M = 0.875, the separation location merges with the shock foot location, which allows unsteadiness in the recirculation region to directly influence the shock behavior. Despite this, it appears the merging does not influence the average shock location. The reattachment location exhibits a strong Mach number dependence; i.e., the recirculation region lengthens with increasing Mach number. There is a slight difference and change in slope between the current data and that of Horstman and Johnson [7], indicating a longer reattachment region. This may be caused by the greater tunnel blockage and resulting impressed pressure gradient in the current experiment. These measurements show that the current experiment faithfully replicates the shock and reattachment behavior observed in earlier experiments. This dataset is planned to be extended in the coming months to include additional Mach numbers, greater resolution of the shock and separation locations, and identification of lower Mach numbers where the flow may remain fully attached.

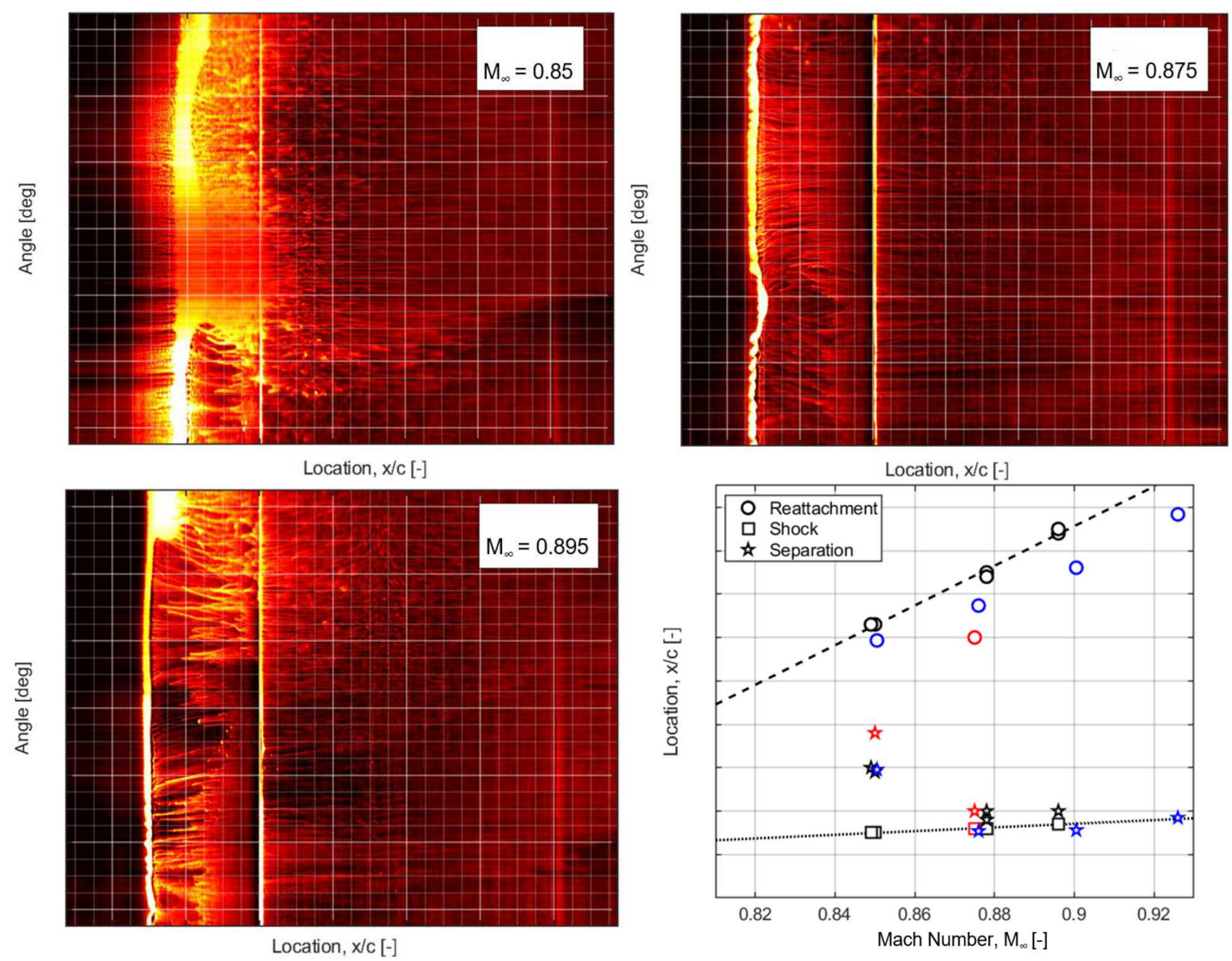

Figure 8. Example oil-flow visualizations. Top row and bottom right, instantaneous snapshots at specified freestream Mach numbers. Bottom right, extracted features: current data (black symbols), Horstman and Johnson [7] (blue symbols) and Bachalo and Johnson [3] (red symbols).

D. Particle Image Velocimetry

Planar particle image velocimetry is used to characterize the tunnel turbulence level, incoming boundary layer, and flow over the hump. The PIV arrangement consists of a LaVision Imager sCMOS camera (2560 x 2160 px at 50 Hz, 6.5 µm pixel size) and a Quantel Evergreen HP laser (2 x 310 mJ/pulse at 25 Hz). Seeding is provided by a Corona Vi-count 5000 thermal smoke generator, producing large quantities of particles of approximately 0.7-0.8 µm diameter as measured in other test campaigns using a shock-wave test.

The small size of the hump and boundary layer require separate high-magnification setups to be adequately resolved. For the incoming boundary layer and turbulence intensity, a Nikon 200mm f/4 Micro-NIKKOR lens and a 2:1 teleconverter provide a magnification of approximately 1.5 (267 px/mm) at a camera working distance of approximately 12 in. To accommodate this short working distance, the optical setup is 'folded' into the tunnel plenum as shown in figure 9, using a large laser line mirror to redirect the image to the camera. The same folded arrangement is used for the wake measurements, but with a 105 mm lens to yield a magnification of 0.4 (64 px/mm).

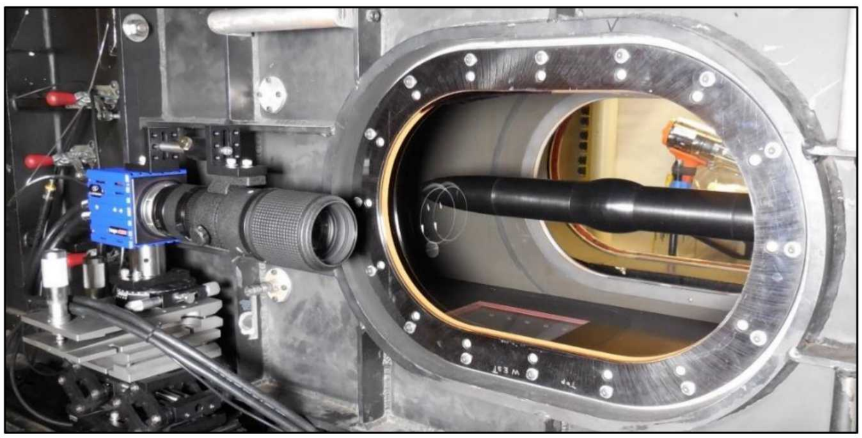

Figure 9. PIV camera arrangement in relation to test section and model. Turning mirror not shown.

The boundary layer measurement is shown in figure 10, and employs the ensemble correlation approach of Meinhart [8] with an integer-shift vibration-reduction to improve the near-wall spatial resolution. The final window size is 16 px x 4 px (60 µm x 15 µm), corresponding to a first unbiased vector occurring at $y^+ \approx 10$. The fit of Sun and Childs [9], valid for compressible boundary layers above the overlap layer, is applied to the data at $y^+ > 50$. The PIV data is spatially-resolved across approximately 8 mm in the streamwise direction, allowing spatially varying BL properties to be evaluated as shown in figure 11.

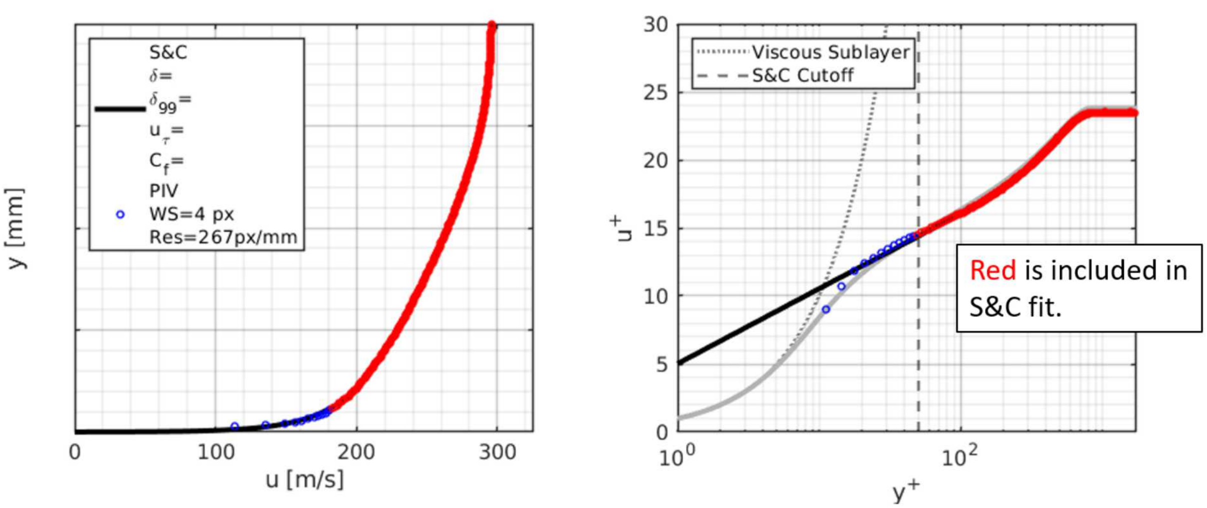

Figure 10. Incoming boundary layer profiles. Left, in physical coordinates. Right, inner variables. Points are from the measurement, with red indicating points used within the S&C fit. Black line indicates S&C fit.

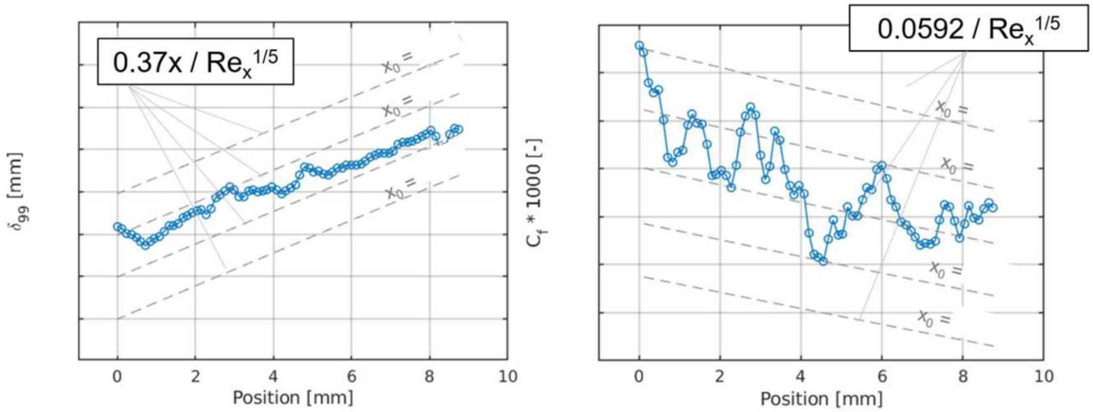

Figure 11. Variation in boundary layer properties as a function of streamwise position. Values of δ_{99} and C_f from the S&C fit at each downstream station. Reference equations are from turbulent flat-plate boundary layer correlations in Schlicting and Gersten [10].

The turbulence intensity measurement was conducted following the method proposed by Scharnowski et al. [11], where multiple measurements at different Δt are used to unambiguously determine turbulence intensity in the presence of measurement noise. Six runs of 500 image pairs each were used to build the required statistics, with processing conducted using an iterative image deformation method with a range of window sizes from 24 px (0.09 mm) to 256 px (0.95 mm) and a suitable initial predictor to capture the large displacements for longer Δt; results are shown in figure 12. The method yields similar turbulence intensity of 0.23% regardless of window size and correctly captures the increase in random noise as the window size is reduced. This dataset is planned to be extended with additional cases at shorter Δt to improve the curve-fitting procedure before reporting the final value of turbulence intensity to be used as a computational input.

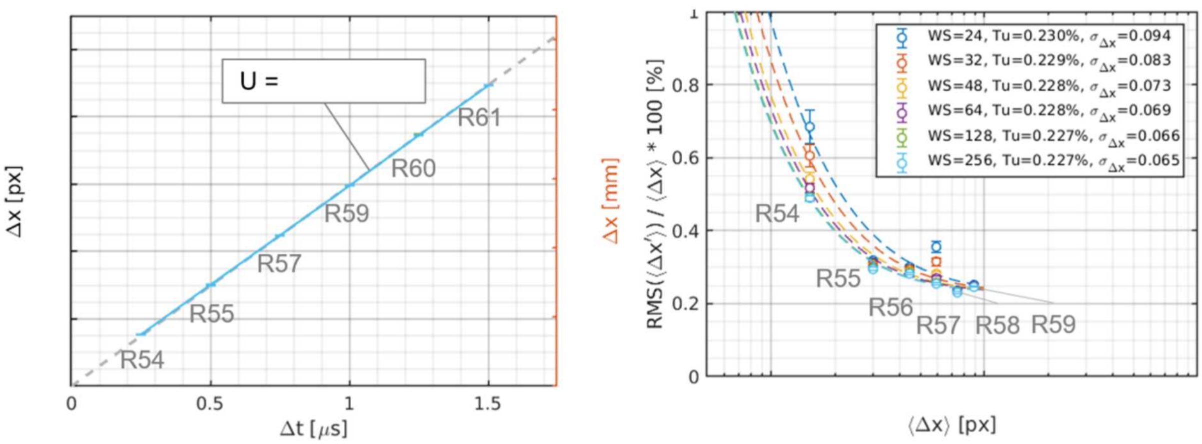

Figure 12. Calculation of turbulence intensity from multiple-Δt data. Left, variation in Δx with increasing Δt. Right, normalized RMS fluctuations of Δx. Dashed lines are from model of Scharnowski et al. [11].

Measurements of the recirculation region were conducted using three separate fields-of-view translated to span from x/c = 0.6 to 1.4, with the statistics of overlapping regions averaged. Three runs of 1000 image pairs each were used to build the statistics for each field-of-view, with processing using an integer-shift vibration correction and iterative image deformation with a window size of 40 px (0.32 mm). The particle image density is approximately 0.008 particles per pixel at this magnification, yielding around 14 particles per interrogation window. Results of this analysis are shown in figure 13.

The shock location is clearly captured, with a signature in both velocity components, and is consistent with the results of the oil-flow visualization. The separation occurs immediately afterwards, resulting in a well-defined shear layer that extends throughout the entire stitched field-of-view. The recirculation region is outlined by a dark contour line indicating u, v = 0 in the respective plots. Again, the reattachment point where is consistent with oil-flow visualization. Note that the separation point as indicated in these plots appears to be shifted downstream with respect to the oil-flow data; this is due to the u, v coordinate system not being body-aligned along the hump. This slightly alters the interpretation of the beginning of the u = 0 region. The evolution of the Reynolds stress throughout the flow is captured, with peak values occurring above the reattachment point. A comparison of these values with example simulation data is shown in the section 4.

These data represent a selection of the data to be available as part of the validation challenge. Additional upstream and downstream measurement planes will be acquired to further characterize the flow, and additional analysis such as vorticity thickness and two-point correlations will establish shear layer growth rates and length scales, respectively. Modal analysis is also to be performed, to identify the dominant scales of their interaction. These quantities will be particularly useful as part of the validation of advanced, scale-resolving simulation methods.

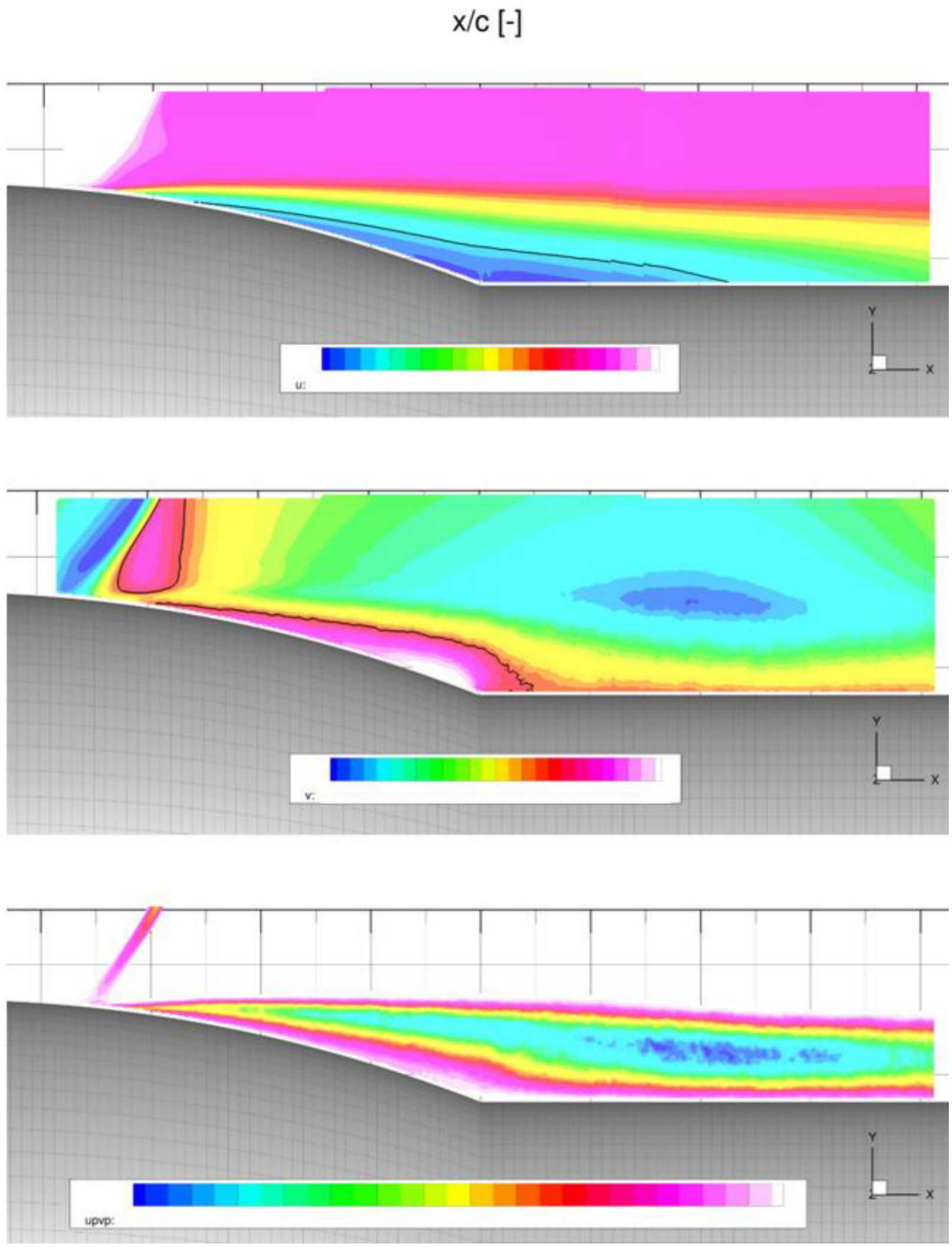

Figure 13. Time-averaged PIV measurements in wake region. Top, u (streamwise) velocity. Middle, v (transverse) velocity, Bottom, u'v' Reynolds stress.

C. Fast Pressure-Sensitive Paint

Fast PSP measurements are to be performed to characterize the mean and unsteady pressure along the model. The pressure fluctuations are estimated to be around 5% and 2.5% of the freestream pressure values at the shock foot and reattachment points, respectively [6]. Measurements are planned with a new formulation of PSP proposed by Egami et al. [12] and recently applied by Lynch et al. [13]. This formulation is brighter than previous ceramic fast PSPs, is easier to apply, and has a lower temperature sensitivity. The time response of the paint is less than 10 µs, providing frequency response up to 100 kHz. This response should be adequate to determine the existence of low-frequency unsteadiness, for example a possible antisymmetric azimuthal mode as observed in axisymmetric step flows by Weiss and Deck [14]. By using two high-speed cameras positioned on both sides of the model, coverage of at least 180 degrees of the model can be achieved. At the time of this paper, these data have not yet been acquired, but are planned as validation data for the simulations submitted for the challenge (see below).

D. Oil-Film Interferometry

Surface shear stress is challenging on this model, as cantilevered-plate or MEMS-style shear stress sensors are not compatible with the significant surface curvature. Therefore oil-film interferometry is planned for measuring the surface shear stress from the beginning of the hump through to the reattachment region. This technique has been successful in numerous configurations, including high-speed compressible flows [15]. It has also been used to provide skin friction data on the NASA 2D hump configuration by Naughton et al. [16]. Again, at the time of this paper, these data have not yet been acquired, but are planned as validation data for the simulations submitted for the challenge (see below).

IV. CFD Comparisons

Analysis of the present experiment has been performed from the beginning of the design process to guide choices in experimental geometry and flow conditions. By performing our own simulations in parallel with the experiments, we can confirm that the validation case is appropriate for assessing modeling performance and to define the experimental data required. The analysis is performed using the SIGMA-CFD code: a multi-block, structured-grid, cell-centered finite volume solver applied to the compressible RANS equations [17]. The results presented to date use the SST-2003 turbulence model [18]. Grid sensitivity studies have been performed, as well as a code-to-code comparison exercise using the data provided on the NASA Turbulence Modeling Resource site [19] for the Bachalo-Johnson flow. CFD analysis has been applied to:

- Confirm the model nose design results in a shock-free shape.
- Study the effects of modifications to the hump geometry.
- Confirm axisymmetry of the surface pressure, near-body mean velocity, and near-body Reynolds stress.
- Assess the effects of boundary layer transition location on the body and estimate the transition location in the experiment by comparing the CFD solutions to the measured mean velocity profile upstream of the hump.
- Assess the effects of test section wall boundary layer transition location on the body surface pressure field and the near-body flow-field.
- Investigate the isolated effect of change in Reynolds number from the Bachalo-Johnson experimental condition to the present condition.
- Investigate flow-field sensitivity to the thermal boundary condition applied on the body surface.
- Aid in identifying the most useful locations for model instrumentation, as well as estimate the range of Reynolds stress magnitudes present to set instrumentation requirements.

A small subset of CFD results is presented here to illustrate its utility within the experimental design process and make some initial comparisons of behavior of the flow-field relative to previous experiments. Two visualizations are shown in figure 14 from RANS calculations for a version of the experimental configuration considered during the design phase. The left image illustrates the achievement of a shock-free nose shape. This was desired to avoid a shock-boundary layer interaction ahead of the hump, which would complicate modeling efforts. The right image shows radial turbulence kinetic energy profiles within the post-shock separation region, each taken at a different azimuth angle, illustrating the presence of noticeable, but small, deviations from axisymmetry caused by the square test section.

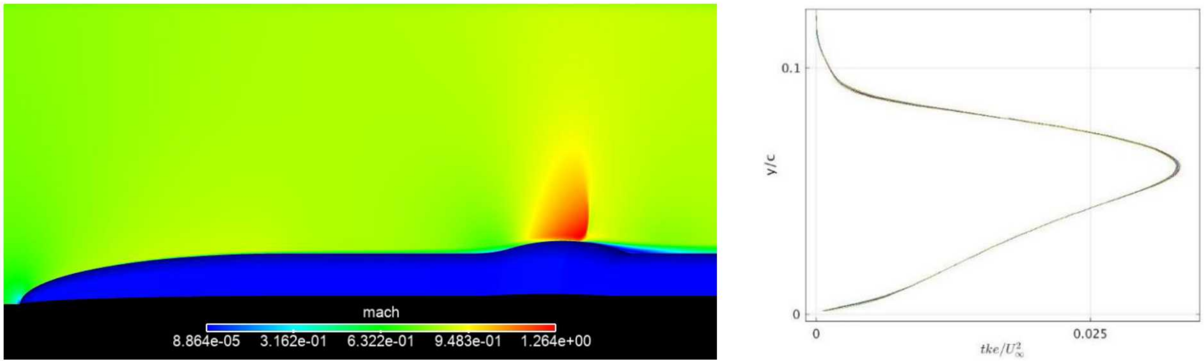

Figure 14. Left, Contours of Mach number for a version of the geometry considered during the design phase. Right, Profiles, taken at different azimuth angles, of turbulence kinetic energy at an axial location within the post-shock separation region.

A comparison is shown in figure 15 shows a comparison between measured mean stream-wise velocity and Reynolds shear stress with RANS results for a particular flow condition. The profiles are located at three different streamwise locations within the separated flow region, downstream of the shock. The profiles exhibit expected qualitative similarity with the previous Bachalo-Johnson flow, while the Reynolds stresses are under-predicted by the SST-2003 model in this instance, consistent with prior experience with the Bachalo-Johnson case (see the results from [19]).

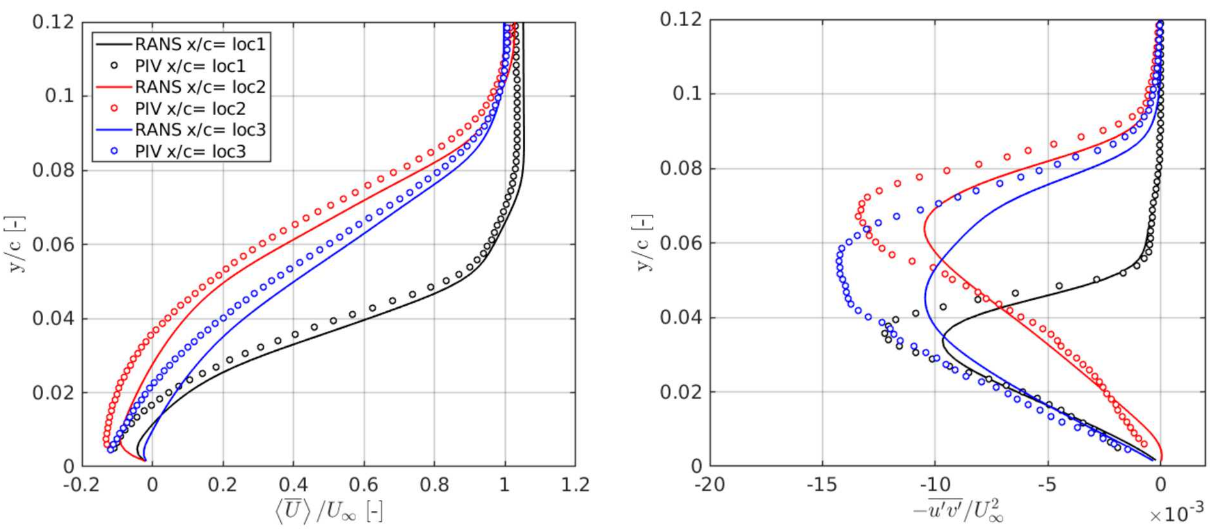

Figure 15. Example comparisons between RANS predictions made with the SST model and present PIV measurements at three streamwise locations within the post-shock separation region. Left, Mean streamwise velocity profiles. Right, Reynolds shear stress profiles.

V. CFD Challenge

The simplicity of the geometry and the desire for additional data expressed by multiple modeling groups motivated us to propose a 'CFD Challenge' to the community. The challenge is 'blind,' in that the model and tunnel geometry, inflow conditions, and tunnel turbulence properties are provided to participants, but the experimental data near the hump is initially withheld. These data describing the unsteady region will be revealed only after all simulations have been completed. The primary goal is to assess various simulation approaches, while preventing a biased evaluation by removing the ability to calibrate a model to the experimental data *a priori*. A secondary goal is to evaluate the variability between CFD estimates when the experimental data is unknown.

The idea of a blind CFD challenge is not new; for example, Klausmeyer and Lin [20] performed a blind comparison of methods for estimating aerodynamic performance of a high-lift airfoil. Simms et al. [21] performed a blind comparison of wind turbine simulation data to experimental data acquired in a collaborative effort between the National Renewable Energy Laboratory and NASA Ames Research Center. Multiple blind comparisons have been performed for laminar, high-enthalpy, hypersonic flow, including Harvey et al. [22], Holden et al. [23], and Holden et al. [24]. Perhaps the best examples of collaborative blind comparisons are the AIAA drag prediction workshops [25] and the high-lift prediction workshops [26], both of which served as excellent forums for assessing the consistency of predictions from numerous contributors and the state of the art in CFD capabilities. From the experimental side, similar challenges such as the international PIV challenges have been valuable for identifying promising algorithms and their effect on acquired data [27].

The present flow case provides a compelling benchmark problem for several reasons. First, the Reynolds number of the flow makes it accessible to the full range of simulation approaches, including DNS. We expect DNS results to greatly aid in ultimate interpretation and understanding of the turbulence model predictions. Further, application of a range of approaches of varying fidelity by different groups, ranging from DNS to wall-modeled LES to RANS, should enhance the communities' understanding of how various modeling choices affect the accuracy of the predictions of different quantities of interest. A successful outcome of this exercise will be not only quantitative assessment of the accuracy of various modeling approaches, but also improved understanding of why the models achieve their level of accuracy. Second, the anticipated fidelity and resolution of boundary condition measurements will reduce uncertainties associated with unknown boundary condition effects that often plague validation studies. The available measurements will also include not only mean flow quantities and Reynolds stresses, but also unsteady surface pressures, thus making the validation exercise highly relevant for those interested in CFD as a tool to predict unsteady, fluid-induced surface loadings.

The challenge organizers will identify specific quantities of interest (QOIs) to be predicted by participants as a basis for model comparison. The QOIs under consideration include those used in past validation studies with the Bachalo-Johnson flow, such as mean velocity and Reynolds stress profiles, mean separation and reattachment locations, and mean surface pressure distribution. The present experiment will add spatial distributions of other single point quantities, such as wall shear stress and surface pressure fluctuation magnitude. We anticipate further comparisons involving spectral information from the wall pressure signal, including temporal and wave-number spectra. We are also exploring QOI's and associated metrics that measure the ability of models to capture topological features of the flow, for example, mean separation bubble volume and separation shear layer vorticity thickness.

The Sandia modeling team already has been simulating this case, both to aid in the experimental design and to test validation methodology. As the Sandia team clearly cannot be considered a 'blind' participant in the validation challenge, this feature will be leveraged as a 'control' group. Sandia's modelers, alone amongst entrants, will have advance access to the final data. Can this allow them to achieve more accurate results? Or will the Sandia simulations return similar accuracy as those modeling teams who are truly blind to the data? This will provide a uniquely useful data point amongst the validation challenge participants.

The challenge is open to any participant, including academic, government, and commercial groups. It is encouraged, but not required, for each participant to submit two entries: first, a RANS-based solution representative of a fast-turnaround engineering analysis; and second, an advanced solution where any method, including DES, LES, or DNS can be used. Once simulation results are submitted, their comparison to the data and the assessment of their performance will be guided by an advisory panel of members external to Sandia whose work does not overlap with groups interested in the Bachalo-Johnson case. This will ensure a neutral appraisal of the models. The timeline of the challenge is tentatively planned as follows:

July 2019, AIAA Aviation (this paper): Formal announcement of the challenge.

January 2020, AIAA SciTech: Publication of geometry details, tunnel model, inflow and turbulence information to the website. Website to be launched allowing potential participants to receive updates and information. Official beginning of the challenge.

Mid-August 2020: Submission deadline for RANS-based entries.

Late September 2020: Submission deadline for advanced simulation entries (DES/LES/DNS).

December 2020: Experimental data to be released at-large on the website.

January 2021, AIAA SciTech: Invited session. 1-2 talks to present the experimental data, 1-2 talks for a comparison to be given by a neutral arbiter (to be determined), and additional talks for participants to describe their simulation approaches and findings.

Acknowledgements

The authors thank Philippe Spalart and Srinivasan Arunajatesan for numerous discussions which led to the selection of this test case and conditions.

References

[1] J. Slotnick, A. Khodadoust, J. Alonso, D. Darmofal, W. Gropp, E. Lurie and D. Mavriplis, "CFD Vision 2030 Study: A Path to Revolutionary Computational Aerosciences," NASA Report CR–2014-218178, 2014.

[2] J. DeBonis, C. Rumsey and M. Malik, "Test Cases for NASA's Revolutionary Computational Aerosciences Technical Challenge," January 2015. [Online]. Available: https://turbmodels.larc.nasa.gov/StandardTestCasesFinal5.pdf.

[3] W. D. Bachalo and D. A. Johnson, "Transonic, Turbulent Boundary-Layer Separation Generated on an Axisymmetric Flow Model," *AIAA J,* pp. 437-443, 1986.

[4] P. Spalart, K. Belyaev, A. Garbaruk, M. Shur, M. Strelets and A. Travin, "Large-eddy and Direct Numerical Simulations of the Bachalo-Johnson flow with Shock-Induced Separation," *Flow Turb Combust,* vol. 99, pp. 865-885, 2017.

[5] C. L. Rumsey, T. B. Gatski, W. L. Sellers III, V. N. Vatsa and S. A. Viken, "Summary of the 2004 Computational Fluid Dynamics Validation Workshop of Synthetic Jets," *AIAA J,* vol. 44, no. 2, pp. 194-207, 2006.

[6] A. Uzun and M. Malik, "Wall-Resolved Large-Eddy Simulations of Transonic Shock-Induced Flow Separation," *AIAA J,* vol. 57, no. 5, 2019.

[7] C. C. Horstman and D. A. Johnson, "Prediction of transonic separated flows," *AIAA J,* vol. 22, no. 7, pp. 1001-1003, 1984.

[8] C. D. Meinhart, S. T. Wereley and J. G. Santiago, "A PIV algorithm for estimating time-averaged velocity fields," *Journal of Fluids Engineering,* vol. 122, no. 2, 2000.

[9] C. Sun and M. E. Childs, "A modified wall wake velocity profile for turbulent compressible boundary layers," *Journal of Aircraft,* 1973.

[10] H. Schlicting and K. Gersten, Boundary-layer theory, Springer, 2016.

[11] S. Scharnowski, M. Bross and C. J. Kahler, "Accurate turbulence level estimations using PIV/PTV," *Experiments in Fluids,* vol. 60, no. 1, 2019.

[12] Y. Egami, Y. Sato and S. Konihsi, "Development of Sprayable Pressure-Sensitive Paint with a Response Time of Less Than 10 μs," *AIAA Journal,* pp. 1-6, 2019.

[13] K. P. Lynch, E. M. Jones and J. L. Wagner, *Simultaneous PSP and DIC measurements for fluid-structure interactions in a shock tube,* AIAA Paper 2018-3870.

[14] P. Weiss and S. Deck, "Control of the antisymmetric mode (m=1) for high Reynolds axisymmetric turbulent separating/reattaching flows," *Physics of Fluids,* p. 095102, 2011.

[15] J. W. Naughton and M. Sheplak, "Modern developments in shear-stress measurement," *Progress in Aerospace Sciences,* vol. 38, pp. 515-570, 2002.

[16] J. W. Naughton, S. Viken and D. Greenblatt, "Skin-Friction Measurements on the NASA Hump Model," *AIAA J,* vol. 44, no. 6, pp. 1255-1265, 2006.

[17] S. Arunajatesan, M. Ross and T. J. Garrett, *Validation of an FSI Modeling Framework for Captive Carriage Applications,* AIAA Paper 2013-2157.

[18] F. R. Menter, M. Kuntz and R. Langtry, "Ten Years of Industrial Experience with the SST Turbulence Model," *Turbulence, heat and mass transfer,* vol. 4, no. 1, pp. 625-632, 2003.

[19] C. Rumsey, "NASA Turbulence Modelling Resource," [Online]. Available: https://turbmodels.larc.nasa.gov/index.html.

[20] S. M. Klausmeyer and J. C. Lin, "Comparative Results from a CFD Challenge Over a 2D Three-Element High-Lift Airfoil," NASA, 1997.

[21] D. Simms, S. Schreck, M. Hand and L. J. Fingersh, "NREL Unsteady Aerodynamics Experiment in the NASA-Ames Wind Tunnel: A Comparison of Predictions to Measurements," NREL, 2001.

[22] J. K. Harvey, M. S. Holden and T. P. Wadhams, *Code Validation Study of Laminar Shock/Boundary Layer and Shock/Shock Interactions in Hypersonic Flow. Part B: Comparison with Navier-Stokes and DSMC Solutions,* AIAA Paper 2001-1031.

[23] M. S. Holden, T. P. Wadhams and M. MacLean, *Measurements in Regions of Shock Wave/Turbulent Boundary Layer Interaction from Mach 4 to 10 for Open and "Blind" Code Evaluation/Validation,* AIAA Paper 2013-2836.

[24] M. S. Holden, M. MacLean, T. P. Wadhams and A. Dufrene, *Measurements of Real Gas Effects on Regions of Laminar Shock Wave/Boundary Layer Interaction in Hypervelocity Flows for "Blind' Code Validation Studies,* AIAA Paper 2013-2837.

[25] E. N. Tinoco, O. P. Brodersen, S. Keye, K. R. Laflin, E. Feltrop, J. C. Vassberg, M. Mani, B. Rider, R. A. Wahls, J. H. Morrison, D. Hue, C. J. Roy, D. J. Mavriplis and M. Murayama, "Summary Data from the Sixth AIAA CFD Drag Prediction Workshop: CRM Cases," *Journal of Aircraft,* vol. 55, no. 4, pp. 1352-1379, 2018.

[26] C. L. Rumsey, J. P. Slotnick and A. J. Sclafani, *Overview and summary of the third AIAA high lift prediction workshop,* AIAA Paper 2018-1258.

[27] C. J. Kahler, T. Astarita, P. P. Vlachos, J. Sakakibara, R. Hain, S. Discetti, R. La Foy and C. Cierpka, "Main results of the 4th International PIV Challenge," *Exp Fluids,* vol. 57, p. 97, 2016.